Catalysis Letters
https://doi.org/10.1007/s10562-019-02781-z

Influence of ZnO Surface Modification on the Photocatalytic Performance of ZnO/NiO Thin Films

Shanmugapriya Periyannan[1,2] · Laura Manceriu[1] · Ngoc Duy Nguyen[3] · Andreas Klein[2] · Wolfram Jaegermann[2] · Pierre Colson[1] · Catherine Henrist[1] · Rudi Cloots[1]

Received: 11 January 2019 / Accepted: 3 April 2019

Abstract

Charge carrier separation is considered as a key factor in enhancing the photocatalytic process and can be maximized by mitigating surface recombination. Following this idea, the surface of zinc oxide (ZnO) was modified by thermal treatment and nickel oxide (NiO) deposition. The influence of the ZnO thermal treatment and NiO deposition conditions on the ZnO surface chemistry and heterostructure interface properties were investigated by in situ X-ray photoelectron spectroscopy (XPS) and photoluminescence (PL) and correlated to the dye photodegradation efficiency. The XPS analysis confirmed a change of doping of ZnO after thermal treatment, which mainly influenced the developed band bending, and has led to an improved photocatalytic activity. For the same reason, the heterostructures based on the surface cleaned ZnO surface had higher photocatalytic efficiency than the ones based on non-cleaned ZnO. The temperature input during NiO deposition had negligible effect on the heterostructure interface properties. The photocatalytic efficiency did not follow the band bending evolution because of a dominant contribution of charge recombination across the NiO layer as indicated by PL analysis.

Graphical Abstract

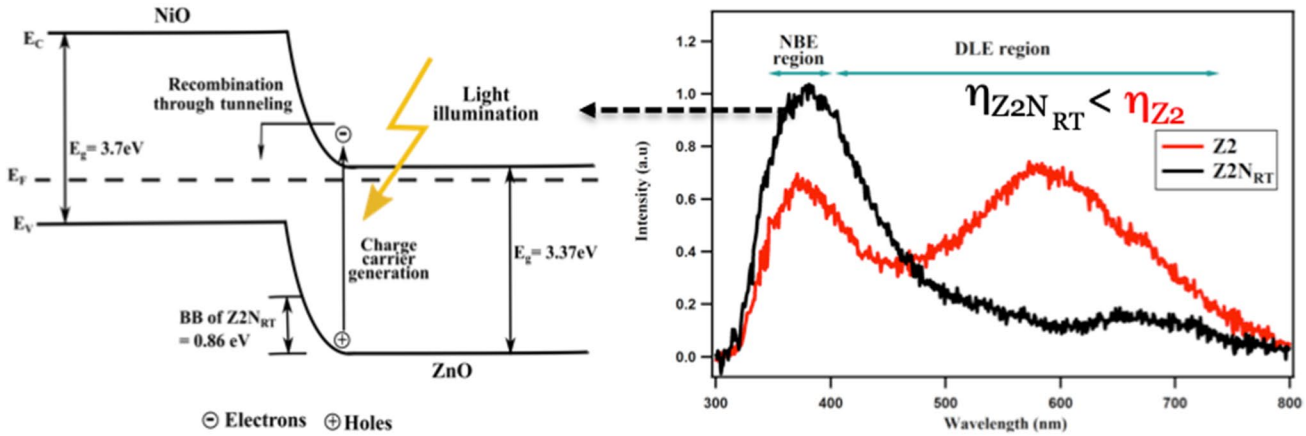

Keywords Heterogeneous catalysis · Catalysis · Thin films · Methodology and phenomena · XPS · Microscopy · Spectroscopy and general characterisation · Photoluminescence · ZnO/NiO · Surface modification · Band bending · Photocatalytic activity

1 Introduction

Nanostructured metal-oxide semiconductors have been widely investigated, being employed in a variety of prospective applications that either address environmental issues or

Electronic supplementary material The online version of this article (https://doi.org/10.1007/s10562-019-02781-z) contains supplementary material, which is available to authorized users.

Extended author information available on the last page of the article

Published online: 17 April 2019

fulfil human needs. Photocatalysis is one among them [1–4]. This process enables the production of electron–hole pairs through light absorption [5]. These photochemical, redox, reactions can be effectively used to tackle environmental problems such as water pollutant degradation, air purification, self-cleaning surfaces or energy generation by water splitting [6, 7]. Metal oxide semiconductors are believed to be promising as photocatalysts since they possess favourable band gap, ideal electronic structure and optical properties. However, their performances as stand-alone materials are limited by the short lifetime of the photo-induced charge carriers [8, 9]. Surface modification techniques like doping, visible light sensitization, metal loading and heterostructure formation are required to overcome these limitations [10].

A typical photocatalytic process involves three vital charge kinetics steps: (i) charge carrier generation, (ii) effective charge transfer and separation and (iii) effective charge consumption [11]. They are interdependent with each other and compromising any of these steps will result in slower kinetics, thereby affecting the efficiency. Therefore, one needs to pay closer attention to the overall structure engineering (surface + interface + band alignment) of the photocatalyst while designing it [12].

Photocatalysts are employed either as powders or thin films based on the requirements. For pollutant degradation, powders have been extensively studied owing to their higher surface to volume (S/V) ratio but they have some limitations such as recombination losses, material recovery and reusability issues [13]. Although thin films do not necessitate a complex retrieval process and allow easy reusability, they suffer from lower S/V ratio. In order to achieve efficient photocatalytic activity in films, surface area needs to be enhanced and one of the strategies is adopting a one-dimension (1D) nanostructure. Also, these structures are advantageous over planar architectures because of the flexibility to tune their dimensions and packing density during growth, they have strong light trapping effect and allow maximizing absorption with much less material [14]. Furthermore, a heterostructured design is required (irrespective of powder or thin films) for boosting the charge separation.

There are several categories of heterostructures or heterojunctions that can be formed: (i) semiconductor–semiconductor (S–S), (ii) semiconductor–metal (S–M), (iii) semiconductor–carbon (S–C) and (iv) multicomponent heterojunction [15].

Zinc oxide (ZnO) is a n-type metal oxide semiconductor, known for its wide bandgap of 3.37 eV and for its unique optoelectronic characteristics like high exciton binding energy of 60 meV, high electron mobility, good thermal stability and better photosensitivity (compared to other semiconductors). Its other advantages include low cost and natural abundance, lack of toxicity, versatility in synthesis and ease of crystallization [16]. Heterostructure formation apart from protecting the ZnO from corrosion, improves the charge separation properties [17, 18]. So far, various metal oxide semiconductors including TiO_2, $BiVO_4$, Fe_2O_3, SnO_2, CdS, Cu_2O and NiO have been used as second material in heterostructures with ZnO either for pollutant degradation or water splitting applications [19, 20]. Nickel oxide (NiO) is a p-type material with a wide bandgap of 3.7 eV and excitation energy of 110 meV with favorable electronic structure and optical properties. It is capable of acting as a good hole transport layer in addition to its ability to act as an electron-blocking layer [21] stirring our choice for the second material. In this study, ZnO nanorods [ZNR] (250–300 nm long and 50–60 nm wide) were hydrothermally grown on F:SnO_2/glass substrates and covered (decorated) by a very thin layer of NiO (< 10 nm) by sputtering, targeting photocatalysis applications. This way of preparing the ZnO/NiO heterostructures was never reported for dyes photodegradation. Li et al. [22] reported the fabrication of NiO/ZnO heterostructures for UV detection applications by sputtering much more thicker NiO (150–450 nm) layers on top of chemically grown ZNR (700 nm long and 50 nm wide). No correlation with a precise application was realized. Echresh et al. [23] prepared ZnO/NiO heterostructures by thermally evaporating NiO (50 nm) onto hydrothermally grown ZnO nanorods. The nanorods were completely covered at the top resulting in an evident loss of specific surface which in exchange did not impact their photoresponse. They correlated the drop in the deep level emission and the constant NBE efficiency with the lower dark current. The improved photocurrent was related to the enhanced charge separation without further insight into the interface properties.

Although ZnO/NiO heterostructures with a structure similar [22–24] or different (planar ZnO-600 nm on top of planar NiO-500 nm [25], ZnO@NiO core–shell heterostructures [18], ZnO/NiO hollow nanofibers [17], flower-like ZnO decorated with cubic NiO particles [26], ZnO/NiO composite (μm range/nm range) powders [27]) than ours were prepared by entirely chemical [18, 24, 26, 27], entirely physical [25] or combined processes [23], most of the time the improvement in the photocatalytic response is more readily related to an enhancement in specific surface. All the previously cited reports fail to simultaneously and comprehensively correlate the photodegradation results with the surface (presence/absence of adsorbates and defects) and interface (Fermi level position, band bending) properties. For example, Ding et al. [18] have prepared ZnO–NiO core–shell heterostructures with high photocatalytic efficiency and reusability via electrochemical deposition on carbon fibre cloth substrates. In this case the variation of the photocatalytic activity with the NiO layer thickness is directly correlated with the specific surface. The reduction in the PL intensity (the deep level emission is not shown) is attributed to the decreased band to band recombination however a measure of

the attained band bending is not given. In another example, ZnO/NiO hollow nanofibers with improved photocatalytic activity [17] were fabricated by impregnating electrospun polyethersulfone (PES) nanofiber webs in nickel and zinc acetate solutions and subsequent thermal treatment. The improved photocatalytic efficiency was attributed to the efficient separation of photogenerated electron–hole pairs without a measure of the attained band bending. Moreover, the difference in specific surface between the composite and the single material fibres is not shown.

Moreover, previous reports on single ZnO or Ag(TiO_2)/ZnO films have often shown a maximum efficiency of 30–40% [28–32].

Since a clean scaffold material is important in order to achieve a high quality interface that will allow effective quantum confinement (an effect, which confines or localizes the movement of electrons as a result of nano scale material) in the heterostructure [33], we have employed a post-processing thermal treatment on ZNR prior to NiO deposition. For the same reason, the deposition conditions for NiO layer were also varied. The correlation of X-ray photoelectron spectroscopy (XPS) and photo luminescence (PL) with the photodegradation results allowed understanding the role of the external factors, like ZnO surface cleaning and NiO deposition conditions, on the scaffold surface chemistry and consequently on the internal factors (band bending, ratio of shallow vs. deep level defects) on the photocatalytic response.

2 Materials and Methods

All the samples were grown on FTO glass substrates purchased from Dyesol (15 W/sq.). Before use, the substrates were cleaned for 15 min each with acetone and then ethanol, by using an ultrasound bath.

2.1 ZnO Nanorod Arrays (ZNR) Preparation by Two-Step Chemical Route

Step 1: Seeding layer preparation: 0.68 g of zinc acetate dihydrate (Sigma Aldrich, 99%) and 225 µL of ethanolamine stabilizing agent, (Sigma Aldrich, 99.5%) were added to 15 mL ethanol (VWR, 99.8%), to result in 250 mM solution. This mixture was stirred at 60 °C for an hour and the stirring was further continued at room temperature (RT), for 24 h. Then 500 µL of the homogeneous solution were spin coated on FTO substrates at 3000 rpm, for 20 s (the relative humidity RH was maintained at 35% during the coating process). This process was repeated 5 times, to ensure complete coverage of the substrate with seeds. The seeded substrates were annealed at 500 °C for 2 h (heating ramp = 300 °C/h).

Step 2: Nanorod growth: 0.072 g of zinc nitrate hexahydrate (Sigma Aldrich, 99%) and 0.052 g of hexamethylenetetramine (Sigma Aldrich, 99.5%) were added to 15 mL of milliQ water and stirred until a homogeneous solution was obtained, which was later transferred to a Teflon lined autoclave. The seeded substrate was immersed in the solution in a tilted position, with the coating facing downward. The hydrothermal process was carried out at 92 °C, for 1 h. Afterwards the samples were washed with distilled water, dried in oven at 60 °C for 30 min and finally annealed at 500 °C for 2 h.

2.2 ZnO Surface Modification

Z1 and Z2 are the ZNR scaffold surfaces without and with surface cleaning treatment respectively. The surface cleaning treatment was carried out inside the sputtering chamber in a controlled, static oxygenated atmosphere (1 h at 400 °C, 0.5 Pa, O_2 flow 5 sccm) for removing the unwanted adsorbates. The ZnO/NiO heterostructured films were prepared by depositing NiO onto scaffold surfaces Z1 and Z2 and the respective samples were denominated as Z1N and Z2N. NiO deposition was done by direct current (DC) magnetron sputtering using a Ni target (99.99% purity), for 40 s, in the presence of argon (Ar) and oxygen (O_2) gases and the substrate was placed at a distance of 9.5 cm from the target and the relative oxygen partial pressure was maintained at 6%. The pressure inside the sputtering chamber was set to 0.5 Pa. Sputtering was performed using a DC power of 40 W, in different temperature conditions: RT deposition, RT deposition followed by post annealing (PA) at 250 °C and high temperature (HT, T = 400 °C) deposition. Correspondingly, the RT, PA and HT indices were added (as subscript) to the sample codes.

2.3 Photodegradation Experiments

All the degradation experiments were carried out with 20 mL ($1.3\ 10^{-6}$ M, i.e. 13 µg) of Rhodamine-B—RhB (Sigma Aldrich, 95%) solution. The prepared substrates were cut into 1 cm × 1 cm that supported around 0.13 mg of ZnO and used in the degradation studies. The ratio between photocatalyst and pollutant used here is 10:1. The ratio usually used for powder photocatalysts is 50:1. Initially, the film was kept under dark for 20 min, with mild stirring, in order to ensure adsorption of pollutants on the surface. It was then exposed to light source for 180 min. Then, 1 mL of aliquot sample was taken at time 0 and then every 20 min and analysed by UV–visible spectrophotometry. This enabled monitoring the pollutant degradation over time and comparing the degradation efficiency of each sample.

2.4 Experimental Methods

The X-ray diffraction patterns of the ZNR films were obtained using the Bruker, D8 Diffractometer equipped with a Cu kα radiation source in the grazing incidence mode (incidence angle 1°) in the 2Θ = 20–70 range. SEM images were acquired using a FEG-SEM (XL 30, FEI) operated at 15 kV. TEM images were obtained by employing a TECNAI G2 TWIN (FEI) operating at 200 kV. PL emission spectra of ZNR and ZnO/NiO films (examined area = 2 cm × 2 cm) were acquired by using a Varian Cary Eclipse, Fluorescence Spectrophotometer equipped with a Xenon flash lamp, which was operated at an excitation wavelength of 325 nm, while emissions were recorded in the range of 300–850 nm. XPS was used to investigate the single/heterostructured films surface and electronic characteristics. The measurements were performed using the Darmstadt Integrated System for Materials Research (DAISY-MAT). It is a physical electronics PHI 5700 multi technique surface analysis system combined with thin film deposition (sputtering, atomic layer) chambers, enabled with a vacuum transfer system. The measurement chamber is equipped with a monochromatic Al Kα X-ray source providing photons with hν = 1486.6 eV. All spectra were measured at a photoelectron take-off angle of 0° (normal emission) and room temperature. Binding energies (BE) of respective elements were obtained calibration with the Fermi edge of sputter cleaned silver (Ag) standard. The Shimadzu UV3600 Plus spectrophotometer was used to measure the absorption spectra of the RhodamineB solution before and after photodegradation.

Degradation studies were carried out under a 5 mW/cm^2 UV light source (maximum wavelength 365 nm), with the sample placed at 18 cm distance from the UV source. RhodamineB (RhB) was used as the model pollutant for investigation. A stock solution of 10 mg/L was prepared and stored in dark. Solution of 1.25 mM was prepared from the stock, to be used during the degradation tests with 1 cm^2 films. The pH was adjusted to 8 for avoiding the dissolution of the ZnO and NiO materials and to render the surface negatively charged (pH > point of zero charge—PZC, ZnO_{PZC} = 8.6–9.2 and NiO_{PZC} = 8.6–10.5 [34], whereas for ZnO heterostructures - PZC = 7.3-7.6[35, 36]) in order to encourage the dye molecules adsorption. Initially the sample was stirred in dark for 20 min to achieve equilibrium and then exposed to UV light for 3 h. The absorption spectra of RhB were registered every 20 min.

3 Results

3.1 X-ray Diffraction

The crystallinity and orientation of the hydrothermally grown ZNR were confirmed with X-ray diffraction (Fig. 1).

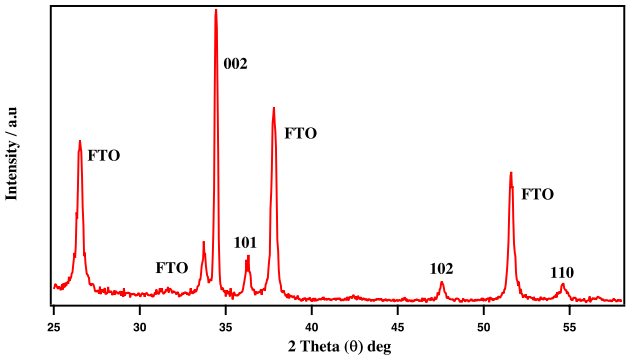

Fig. 1 XRD spectra of ZNR film

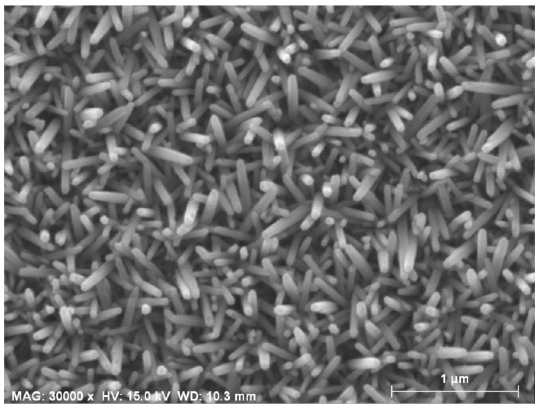

Fig. 2 SEM image of ZNR film

The (002) peak at 2Theta = 34.50° corresponding to the wurtzite phase of ZNR (JCPDS card no. 79-2205) shows the highest intensity, confirming the one dimensional growth along the c-axis as desired.

3.2 Scanning Electron Microscopy

The SEM image of the ZNR showed that densely packed nanorods with random orientation were obtained (Fig. 2). The nanorods were found to be 250–300 nm long and 50–60 nm wide which corresponds to an average aspect ratio of 5. The SEM images of the ZNR film after NiO deposition did not show any changes in the morphology or surface of ZNR. This is due to the fact that the NiO thickness was very low, below 10 nm.

3.3 Transmission Electron Microscopy

The image of Z1 (Fig. 3a) confirms the presence of ZnO 1D nanostructure with smooth surface. Through NiO deposition, the surface of nanorods is uniformly covered with a rough layer (Fig. 3b, c) with a thickness in the range of 2–3 nm.

We also noticed that the thickness of NiO layer was higher for PA than that for RT, which might be due to the supplementary post annealing treatment. The image of HT film (Fig. 3d) revealed the formation of cubic nanoparticles of 5–6 nm (zoomed image in inset of Fig. 3d), rather than a layer at the surface of nanorods. Therefore, this indicates that the crystallite size is enhanced due to the slower growth rate. The (111) plane of NiO could be identified from the TEM images (Fig. S1 in Supplementary Information) for all the samples. The TEM images also demonstrate that the NiO layer was capable of covering the ZNR surface throughout its 200–250 nm length, which would increase the visible light absorption [22].

3.4 Photo Luminescence

The PL spectra of the single ZNR surfaces without and with surface cleaning treatment (Z1 and Z2, respectively) and their corresponding heterostructures with NiO are shown in Fig. 4a, b, respectively. All the spectra exhibited one peak, in the range of 387–397 nm, attributed to Near Bandedge Emission (NBE) [37] which corresponds to the recombination due to surface excitons [38], and another one in the range of 450–800 nm, assigned to deep level emission (DLE) [24, 39] which correspond to the deep trap levels in ZnO (here including O/Zn vacancies and interstitials) [40, 41].

For further understanding the contribution of surface excitons and defects in charge carrier recombination, the intensity ratios I_{NBE}/I_{Total} and I_{DLE}/I_{Total} were determined and given in Table 1. For both Z1 and Z2 scaffold, the DLE emission seems to be predominant in the PL spectra (as seen in Table 1). However with surface cleaning, the NBE emission was mildly reduced with respect to the DLE [42, 43] (see Table 1), proving the removal of adsorbates. A higher difference was expected but not observed, due to –OH readsorption from the ambience while the sample was transferred to the PL instrument [44, 45]. Also, the concentration of deep level defects was slightly reduced since part of the oxygen vacancies were passivated through surface cleaning [46, 47]. In addition, the blue shift of DLE peak after thermal treatment (from 602 nm for Z1 to 584 nm for Z2)

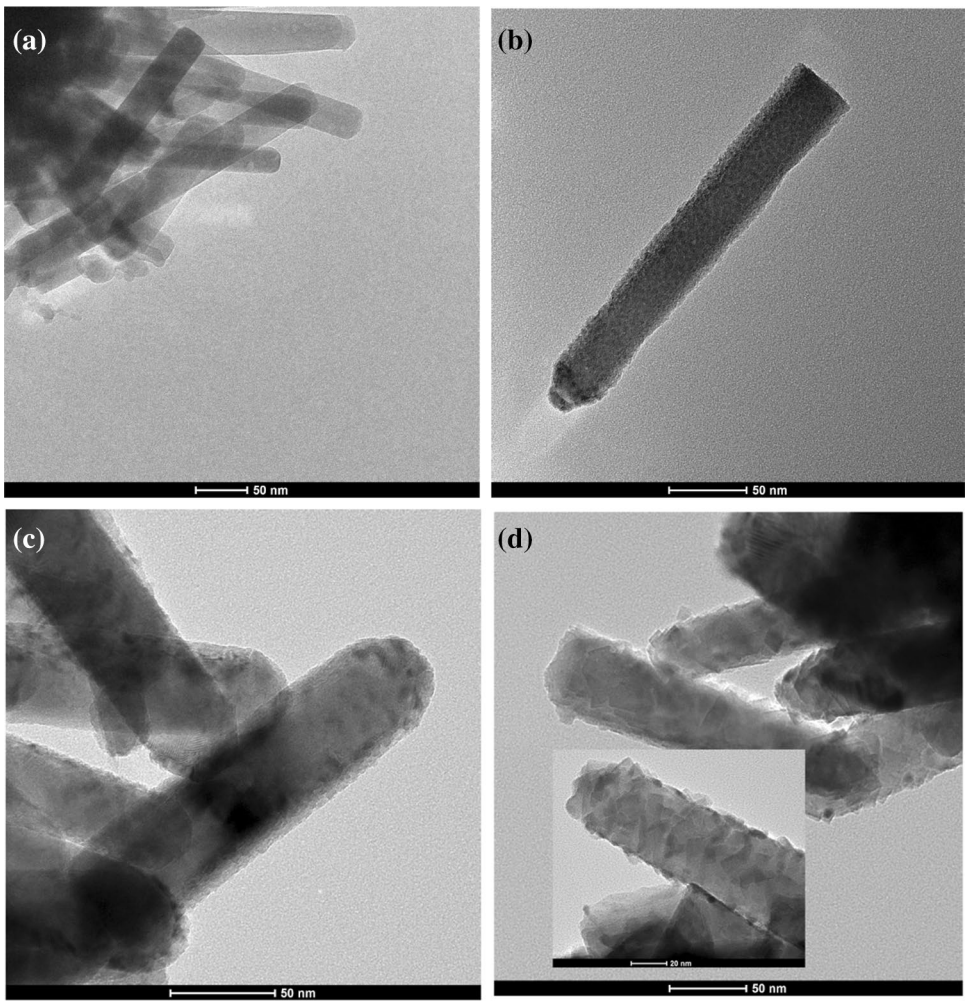

Fig. 3 TEM image of **a** Z1 (without surface cleaning), **b** $Z1N_{RT}$, **c** $Z1N_{PA}$ and $Z1N_{HT}$ [zoomed view in the inset]. *RT* room temperature, *PA* post annealed, *HT* high temperature

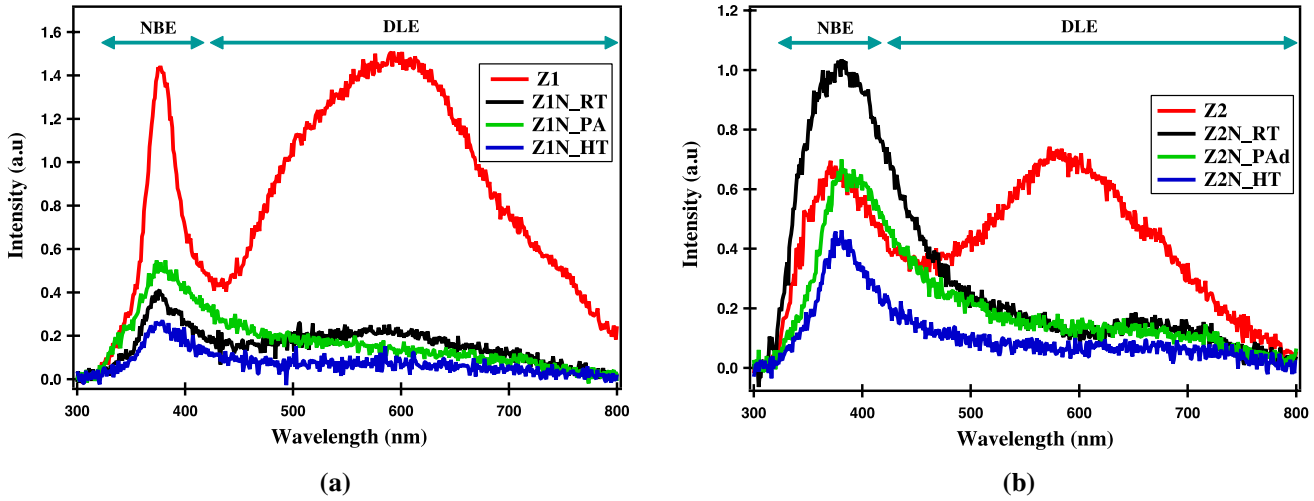

Fig. 4 Photo luminescence spectra of **a** Z1 (without surface cleaning) and corresponding heterostructures and **b** Z2 (surface cleaned) and corresponding heterostructures

Table 1 Sample codes and corresponding details from PL spectrum and band bending values from XPS spectrum [deduced as detailed in (Sect. 3.5)]

Sample code	NBE peak maximum position (in nm)/shift	FWHM of NBE peak (in nm)	I_{NBE}/I_{Total}	I_{DLE}/I_{Total}	Band bending from XPS–V_{bb} (in eV)
Without surface cleaning (Z1)					
Z1	371	38	0.18	0.82	–
$Z1N_{RT}$	379/Red	50	0.05	0.11	1.12
$Z1N_{PA}$	381/Red	61	0.08	0.08	1.32
$Z1N_{HT}$	379/Red	58	0.04	0.03	0.89
Surface cleaned (Z2)					
Z2	367/Blue	40	0.28	0.71	0.50
$Z2N_{RT}$	372/Red	77	0.45	0.34	0.86
$Z2N_{PA}$	381/Red	48	0.1	0.4	0.79
$Z2N_{HT}$	380/Red	41	0.1	0.11	0.67

I_{NBE} and I_{DLE} values were taken by calculating the corresponding area below the deconvoluted peaks (using a data analysis software, IgorPro). RT—deposited at room temperature; PA—deposited at RT and post annealed at 250 °C for 1 h; HT—deposited at high temperature—400 °C]

suggests that part of the V_O were ionized through surface cleaning [43, 48–51].

After NiO deposition the intensity of the PL decreased but with a matching contribution from both DLE and NBE (Table 1), suggesting that even if charge separation was enabled, non-radiative recombination across the NiO layer might have occurred. The NBE peaks of all heterostructures were red shifted (Table 1) signifying an enhancement in the quantum confinement effect [39, 52], as a result of nanoscale NiO covering.

In case of sample $Z2N_{RT}$, the red shift and the increase in intensity of NBE peak might indicate an additional effect, apart from the non-radiative recombination across the NiO layer. Additionally, the broadening of the NBE peak (Table 1) as compared to scaffold indicates the presence of fluctuations at the interface [53, 54]. This effect was removed by using a cleaned scaffold and NiO deposition at HT, as in the case of sample $Z2N_{HT}$.

3.5 X-ray Photo Electron Spectroscopy

As expected, the XPS survey spectra of Z1, Z2 and their corresponding heterostructures (Figure S2 in Supplementary Information) showed the presence of Zn, Ni and O, but also of carbon and hydroxyl species adsorbed on the surface of the Z1 sample [26, 48, 55]. The detailed XPS spectra of Zn2p, Ni2p, O1 s lines and valence band for all the samples are shown in Fig. 5 and Figure S3 in Supplementary Information. The spectra of ZnO after synthesis (Z1) and after surface cleaning (Z2) are overall very similar to each other

showing clearly developed Zn2p and O1s lines (Fig. 5a, b and Table S1 in Supplementary Information) and a valence band structure (Fig. 5g), which indicates the formation of ZnO [25]. The shoulder in the O1s line (Fig. 5b, f) at the binding energy (BE) of 532 eV is attributed to –OH adsorbates [48, 56]. A slight shift of the Zn2p BE of about 0.48 eV (Fig. 5a and Table S1 in Supplementary Information) as well as of the Fermi level (for Z1, $E_F - VBMx = 3.47$ eV whereas for Z2, $E_F - VBMx = 3.04$ eV, Table S1 in Supplementary Information) after surface cleaning (by heating at 400 °C) was observed. These shifts are attributed to a change in the doping of the sample from a sample which was n+ doped

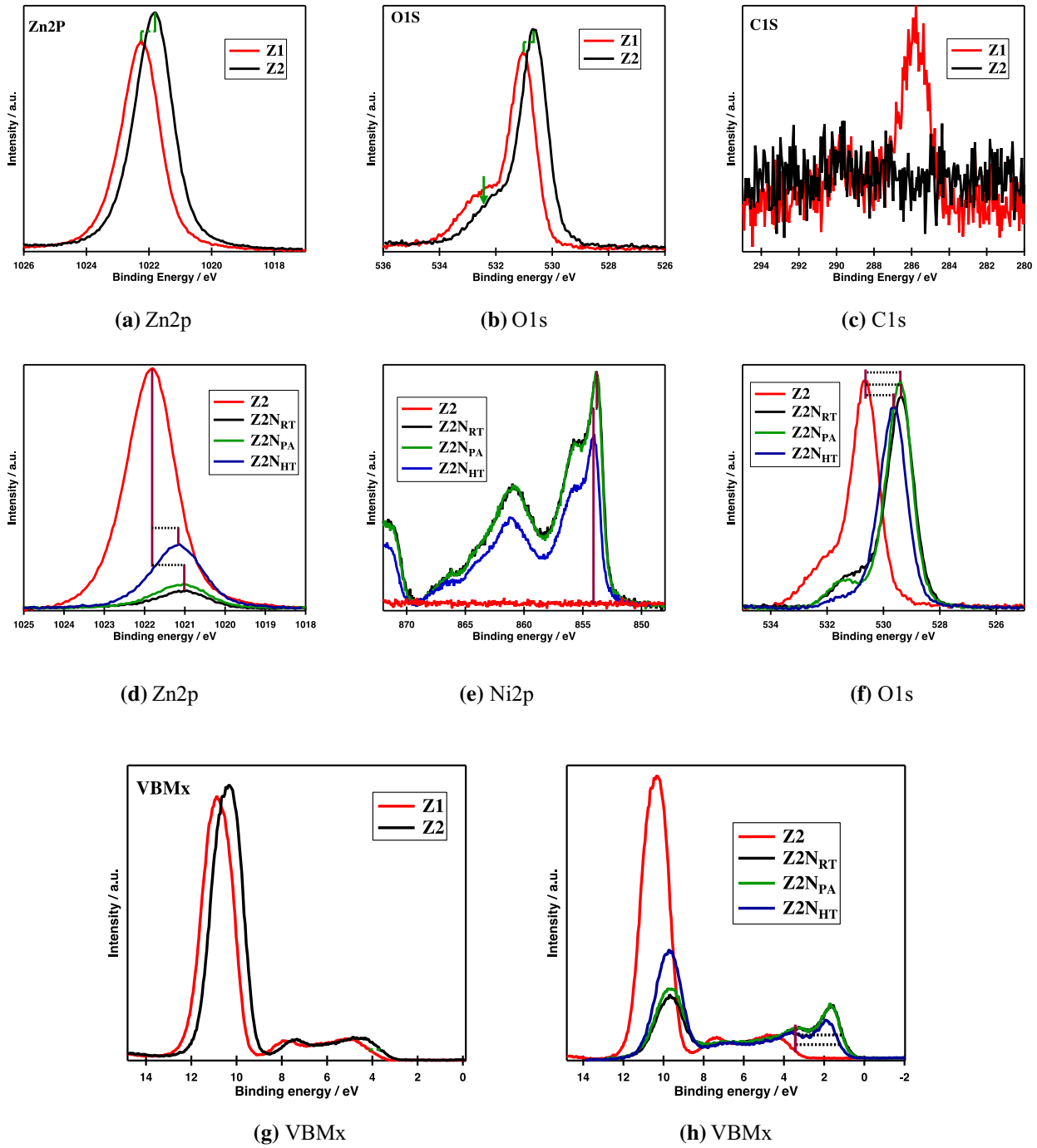

(a) Zn2p **(b)** O1s **(c)** C1s

(d) Zn2p **(e)** Ni2p **(f)** O1s

(g) VBMx **(h)** VBMx

Fig. 5 Zn2p (**a**), O1s (**b**), C1s (**c**) spectra and VBMx (**g**) shift for Z1 (without surface cleaning) and Z2 (surface cleaned) scaffold and Zn2p (**d**), Ni2p (**e**), O1s (**f**) spectra and VBMx (**h**) shift for the Z2 (surface cleaned) scaffold compared with its corresponding heterostructures. *RT* room temperature; *PA* post annealed, *HT* high temperature

to a sample which is n− doped. In principle, we cannot discriminate in these experiments a bulk doping from a surface doping but assume a change of bulk doping because of the small thickness of the nanorods (diameter ≈ 50–60 nm). The increase in intensity of all peaks, the absence of carbon peak and reduction of intensity in the oxygen shoulder peak for Z2 compared to Z1 (Fig. 5a, c) confirmed the effective removal of adsorbents (–OH) through surface cleaning [56].

The shift in VBMx binding energy (Fig. 5g, h) revealed that the Fermi level was positioned above the conduction band (CB) for Z1 (without surface cleaning, $E_F - VBMx = 3.47$ eV, Table S1 in Supplementary Information) and it was shifted below CB ($E_F - VBMx = 3.04$ eV) after surface cleaning treatment (for Z2) in the presence of oxygen. This clearly indicates that part of the oxygen vacancies in Z1 (without surface cleaning) were filled by incoming oxygen (Eq. 1) in case of Z2 (surface cleaned) sample [57, 58].

$$\frac{1}{2}O_2(\text{gas}) + V_O^{++} \rightarrow O_O^x + 2h^{\bullet} \quad (1)$$

With the deposition of NiO, the typical features and satellite structure of Ni^{2+} and O were observed [25] (Fig. 5e, f and Figures S3b and S3c in Supplementary Information). Also, the XPS valence band feature shows the typical spectral signature of NiO (Fig. 5h and Figure S3d in Supplementary Information). However, even for HT conditions, no modification of the satellite peak is detected (Fig. 5e and Figure S3b in Supplementary Information), meaning that the formation of Ni^{3+} is likely improbable.

Band bending (V_{bb}) of the substrate was determined using the Eq. 2 [59–62], that involved subtraction of core level binding energies of substrate or scaffold material (here, Zn2p) at initial step [BE_{Zn2p} (i)) and after surface modification or growing of the NiO film (BE_{Zn2p} (f)]. The V_{bb} values are given in Table 1.

$$V_{bb} = BE_{Zn2p}(i) - BE_{Zn2p}(f) \quad (2)$$

If we compare the observed changes in V_{bb} as well as the changes in relative intensities [25] of Zn2p peak (Table S1 in Supplementary Information) after NiO deposition (Fig. 5d–f and Figure S3a to S3c in Supplementary Information), a clear trend cannot be extracted that could be related to modification of the growth process of the co-catalyst, neither to changes in the doping of the scaffold. However, some general conclusions can be deduced. The overall shift in BE that led to a larger band bending for the Z1 heterostructures as compared to the Z2 ones, due to its higher n+ doping. The NiO deposition at high temperatures on Z1 and Z2 scaffold shows a larger $E_F - VBMx$ difference (0.84–0.95 eV, Table S1 in Supplementary Information) compared to RT and PA depositions (0.66 eV, Table S1 in Supplementary Information), which can be related to a better-defined stoichiometry. Overall, a clearly developed band bending ranging from 1.3 to 0.7 eV (Table 1) is found after NiO deposition.

3.6 Pollutant Degradation

The degradation efficiency for each sample (after 180 min) was calculated according to Eq. 3 and shown in Fig. 6. The evolution of C_t/C_0 as function of time is shown in Figure S4 in Supplementary Information.

$$Efficiency\,(n)\% = \left(1 - \left(\frac{C_t}{C_0}\right)\right) \times 100 \quad (3)$$

where C_t is the concentration in time; C_0 is the initial concentration. The photocatalytic control experiment was carried in light in the presence of Rhodamine-B, without photocatalyst. After exposure in UV light for 180 min. No signs of degradation were observed (Fig. S5 in Supplementary Information).

Z1 was able to degrade 54% of the pollutant whereas, its heterostructures were found to have lower performance, except for HT whose efficiency was 58%. We believe that four competing mechanisms influence the photodegradation efficiency: (1) the holes photogeneration which is favoured for low NiO thickness, (2) charge recombination which is expected to be enhanced when V_{bb} is reduced, (3) ZnO interface charge recombination because of defects and (4) charge recombination across the NiO layer. Though the variation of photocatalytic efficiency in Z1 heterostructures cannot

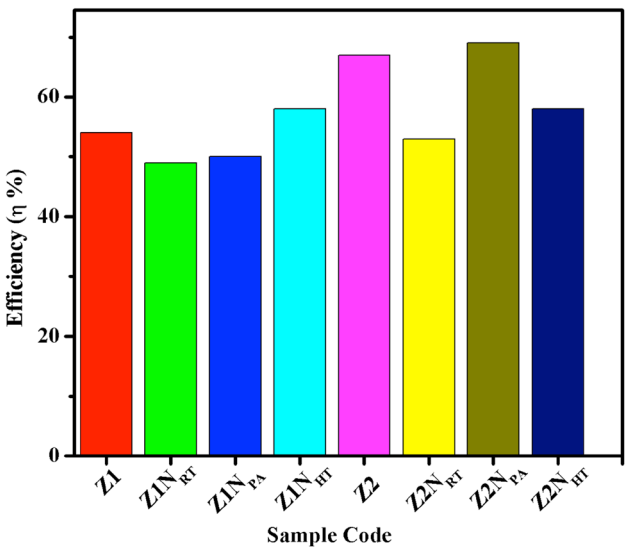

Fig. 6 Pollutant degradation efficiencies of Z1 (without surface cleaning), Z2 (surface cleaned) and their corresponding heterostructures. Degradation study was conducted for three samples of scaffold Z1 (without surface cleaning) and resulted in an error bar of 2%. *RT* room temperature, *PA* post annealed, *HT* high temperature

be explained by a simple combination of these arguments, it is obvious in case of sample $Z1N_{HT}$ that mechanism (1) is prevailing. Concurrently, the Z2 heterostructures were overall more efficient than their Z1 counterparts, with the highest efficiency obtained for the $Z2N_{PA}$ (69%) but with similar activity with the Z2 scaffold. From here we conclude that limiting the contribution of mechanism (3) by surface cleaning is mostly influencing the photocatalytic efficiency and the modest or lack of improvement after NiO deposition might be influenced by mechanism (4), which could be due to a thin space charge layer.

Recent reports have demonstrated that post processing of ZnO or heterostructure formation enhanced photocatalytic activity due to reduction in surface/bulk defects and improved charge separation [14, 15]. This was also correlated with the photoluminescence response but with inconsistent conclusions; reduction [30, 63, 64] and increase [22, 38] in the NBE emission were both related to an enhancement in photocatalytic activity. The PL, XPS and RhB photodegradation allowed us to conclude that in order to obtain a better efficiency, charge separation should be effective (high band bending) which is correlated to the PL emission diminution but also to non-radiative recombination across NiO layer should be avoided by increasing the width of the space charge layer.

4 Discussion

The XPS measurements of Z1, Z2 and their respective heterostructures (Fig. 5 and Supplementary Figure S3) have been used to determine the Fermi level positions and band bending attained for each sample. In case of Z1 scaffold the position of the Fermi level is above the CB (Fig. 7a) which causes a downward band bending and thus the formation of an e^- accumulation layer. In case of the Z2 scaffold the Fermi level position was shifted below CB after surface cleaning treatment (Fig. 7b), followed by band flattening due to e^- depletion [51].

Bringing n-type ZnO and p-type NiO material into contact resulted in the formation of a space charge region at the interface and thus band bending (example shown for $Z2N_{RT}$ in Fig. 7c, $E_F - VBMx$ values from Table S1 in Supplementary Information). The maximum band bending obtained for Z1 heterostructures was 1.3 eV, higher than for Z2 heterostructures (0.86 eV). However, the pollutant degradation process emphasized that larger band bending does not generally lead to higher photodegradation efficiency.

These results might be in contrary to previous literature reports where heterostructures were shown to be

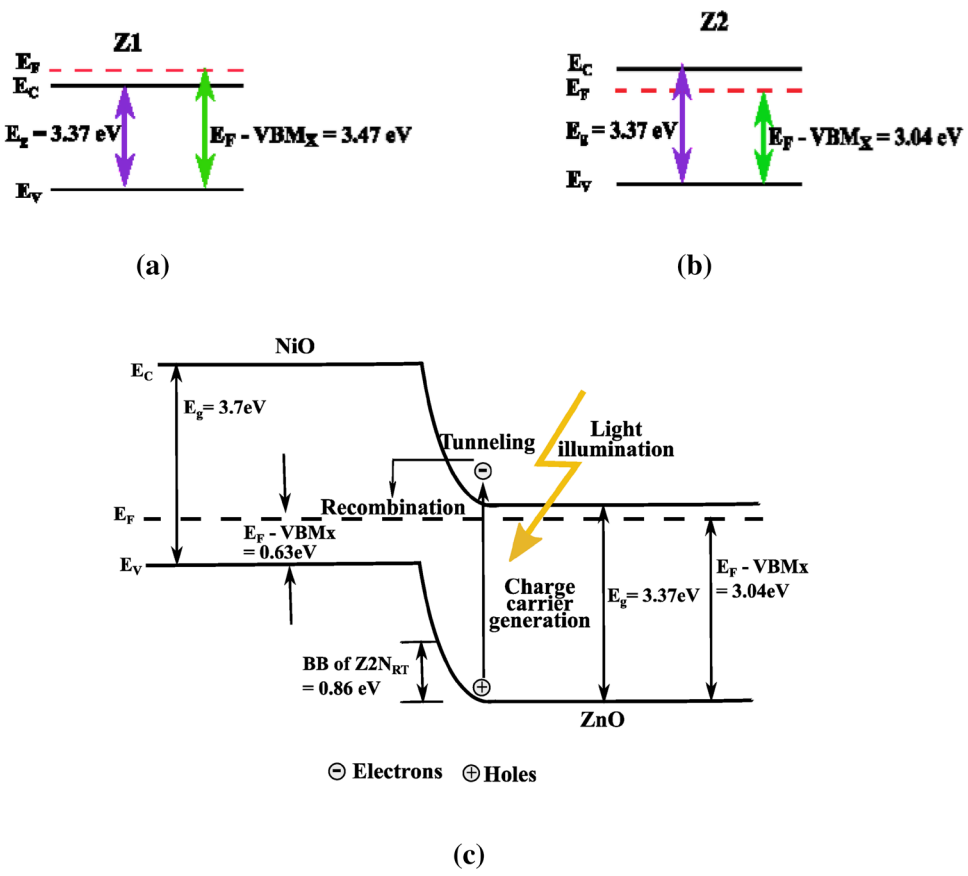

Fig. 7 Band energy diagram of Z1—without surface cleaning (**a**) and Z2—surface cleaned (**b**), band alignment and band bending for $Z2N_{RT}$ (**c**) [*RT* room temperature]. $E_F - VBMx$ values as obtained from the respective XPS spectra

photocatalytically more active as a consequence of charge separation induced by interfacial band bending [14, 15]. The optimal band bending (height and width of the space charge layer) and its influence on photocatalytic response were not reported in literature previously. Thus, for a detailed discussion of space charge layer effects in charge carrier separation, all aspects of heterostructure preparation must be taken into consideration. Due to the high doping of the ZnO scaffold, which is an indication of large concentration of bulk/surface defects, the width of the space charge layer shown in Fig. 7c is very small. As a consequence, charge carriers are not evidently separated due to the contact but instead recombine via the NiO layer by tunnelling through the extremely thin interface barrier. This mechanism can explain the low catalytic efficiencies obtained for Z1 based samples and the modest improvement in the efficiencies of Z2 samples as here the doping concentration is reduced.

These conclusions are also supported by the PL data, represented in Sect. 3.4. In all samples we observe a high contribution of defect states as recombination centers. These defect states may also be involved in the electron–hole recombination across the NiO contact layer due to increased rate of electron transfer across the space charge layer. The strong reduction in the overall photoluminescence intensity after NiO deposition, but with an almost equal contribution from deep level and surface defects (Table 1), can also be taken as clear argument for the above formulated hypothesis describing a dominating influence of electron–hole recombination vs. electron–hole separation.

In conclusion, our results indicate that there is a fine balance between appropriate band bending, a good quality interface and the reduction of charge recombination. Such a balance was only attained for the Z2 samples mainly as a result of surface cleaning treatment, with little influence from the NiO deposition conditions due to recombination across the NiO layer.

5 Conclusion

ZnO surface was modified by heat treatment in O_2 atmosphere and then sputtered NiO (p-type) onto chemically grown 1D ZnO (n-type). The influence of ZnO surface cleaning and NiO deposition conditions on the heterostructure formation and final performance in dye degradation was studied. The XPS study of the bare ZnO revealed that the Fermi level of the as-prepared ZnO surface which was above the conduction band (CB) shifted inside the bandgap after surface cleaning treatment. This confirms that the doping of ZnO was changed but the PL results alone cannot discriminate if this has taken place at the surface or in the bulk. By correlating XPS and PL with the photodegradation activity we were able to conclude that the improved photo-catalytic performance of Z2 samples compared their Z1 counterparts was mostly the consequence of surface cleaning. Indeed, the modest performance of the heterostructures compared to the scaffolds indicates that the charge separation after NiO deposition was not as effective as it would have been expected from the band bending values (V_{bb} in the range of 0.7 to 1.3 eV) because of charge recombination inside the NiO layer (PL results show that DLE and NBE contributions were equally present no matter the deposition conditions). The highest photocatalytic efficiency among the Z2 heterostructures was obtained for sample $Z2N_{PA}$ for which the developed NiO layer thickness allowed the mitigation of the tunnelling effect. Therefore our study demonstrates that the correlation of a high band bending or PL emission quenching/increase with the improved photocatalytic efficiency is not straightforward and other factors must be considered when tuning the band bending such as the materials doping level, the space charge layer thickness, the co-catalyst thickness, etc., in order to maximize the photocatalytic efficiency.

Acknowledgements This work was carried out in the framework of EJD-FunMat (European Joint Doctorate for Multifunctional Materials) and has received funding from the European Union's Horizon 2020 research and innovation programme under the Marie Sklodowska Curie Grant Agreement No. 641640.

Compliance with Ethical Standards

Conflicts of interest The authors declare no conflict of interest.

References

1. Vinodgopal K, Bedja I, Kamat PV (1996) Nanostructured semiconductor films for photo-catalysis. Photoelectrochemical behavior of SnO_2/TiO_2 composite systems and its role in photocatalytic degradation of a textile azo dye. Chem Mater 8:2180–2187
2. Hoffmann MR, Martin ST, Choi W, Bahnemann DW (1995) Environmental applications of semiconductor photocatalysis. Chem Rev 95(1):69–96
3. Fernandez´-Garcia M, Martinez-Arias A, Hanson JC, Rodriguez JA (2004) Nanostructured oxides in chemistry: characterization and properties. Chem Rev 104:4063–4104
4. Khan MM, Adil SF, Al-Mayouf A (2015) Metal oxides as photocatalysts. J Saudi Chem Soc. https://doi.org/10.1016/j.jscs.2015.04.003
5. Serpone N, Emeline AV (2005) Modelling heterogeneous photocatalysis by metal-oxide nanostructured semiconductor and insulator materials: factors that affect the activity and selectivity of photocatalysts. Res Chem Intermed 31:391–432
6. Ibhadon A, Fitzpatrick P (2013) Heterogeneous photocatalysis: recent advances and applications. Catalysts 3:189–218
7. Ameen S, Akhtar MS, Seo HK, Shin HS (2014) Metal oxide semiconductors and their nanocomposites application towards photovoltaic and photocatalytic. Adv Energy Mater. https://doi.org/10.1002/9781118904923.ch3
8. Mondal K, Sharma A (2016) Recent advances in the synthesis and application of photocatalytic metal-metal oxide core-shell

nanoparticles for environmental remediation and their recycling process. RSC Adv 6:83589–83612
9. Bai S, Yin W, Wang L, Li Z, Xiong Y (2016) Surface and interface design in cocatalysts for photocatalytic water splitting and CO_2 reduction. RSC Adv 6:57446–57463
10. Meng NKS, Leung MKH, Leung DYC (2007) A review and recent developments in photocatalytic water-splitting using TiO_2 for hydrogen production. Renew Sustain Energy Rev 11:401–425
11. Bai S, Jiang W, Li Z, Xiong Y (2015) Surface and interface engineering in photocatalysis. ChemNanoMat 1:223–239
12. Bai S, Jiang J, Zhang Q, Xiong Y (2015) Steering charge kinetics in photocatalysis: intersection of materials syntheses, characterization techniques and theoretical simulations. Chem Soc Rev 44:2893–2939
13. Ali AM, Emanuelsson EAC, Patterson DA (2011) Conventional versus lattice photocatalysed reactions: implications of the lattice oxygen participation in the liquid phase photocatalytic oxidation with nanostructured ZnO thin films on reaction products and mechanism at both 254 nm and 340 nm. Appl Catal B Environ 106(3–4):323–336. https://doi.org/10.1016/j.apcatb.2011.05.033
14. Liu S, Han C, Tang Z-R, Xu Y-J (2016) Heterostructured semiconductor nanowire arrays for artificial photosynthesis. Mater Horiz 3(4):259–364
15. Wang JLH, Zhang L, Chen Z, Hu J, Li S, Wang Z, Wang X (2014) Semiconductor heterojunction photocatalysts: design, construction, and photocatalytic performances. Chem Soc Rev 43:5234–5244
16. Klingshirn C (2007) ZnO: from basics towards applications. Phys Status Solidi (B) Basic Res 244(9):3027–3073
17. Li J, Zhao F, Zhang L, Zhang M, Jiang H, Li S, Li J (2015) Electrospun hollow ZnO/NiO heterostructures with enhanced photocatalytic activity. RSC Adv 5:67610–67616
18. Ding M, Yang H, Yan T, Wang C, Deng X, Zhang S, Huang J, Shao M, Xijin X (2018) Fabrication of hierarchical ZnO@NiO core–shell heterostructures for improved photocatalytic performance. Nanoscale Res Lett 13:260
19. Kumar SG, Rao KS (2015) Zinc oxide based photocatalysis: tailoring surface-bulk structure and related interfacial charge carrier dynamics for better environmental applications. RSC Adv 5:3306–3351
20. Lee KM, Lai CW, Ngai KS, Juan JC (2016) Recent developments of zinc oxide based photocatalyst in water treatment technology: a review. Water Res 88:428–448
21. Irwin MD, Buchholz DB, Hains AW, Chang RPH, Marks TJ (2008) p-Type semi-conducting nickel oxide as an efficiency-enhancing anode interfacial layer in polymer bulk-heterojunction solar cells. Proc Natl Acad Sci 105(8):2783–2787
22. Li YR, Wan CY, Chang CT, Tsai WL, Huang YC, Wang KY, Yang PY, Cheng HC (2015) Thickness effect of NiO on the performance of ultraviolet sensors with p-NiO/n-ZnO nanowire heterojunction structure. Vacuum 118:48–54
23. Echresh A, Chey CO, Shoushtari MZ, Khranovskyy V, Nur O, Willander M (2015) UV photo-detector based on p-NiO thin film/n-ZnO nanorods heterojunction prepared by a simple process. J Alloy Compd 632:165–171
24. Vijayaprasath G, Sakthivel P, Murugan R, Mahalingam T, Ravi G (2016) Deposition and characterization of ZnO/NiO thin films. AIP Conf Proc 1731:080033
25. Deng R, Yao B, Li YF, Zhao YM, Li BH, Shan CX, Zhang ZZ, Zhao DX, Zhang JY, Shen DZ, Fan XW (2009) X-ray photoelectron spectroscopy measurement of n-ZnO/p-NiO heterostructure valence-band offset. Appl Phys Lett 94(2):022108-1–022108-3
26. Tian F, Liu Y (2013) Synthesis of p-type NiO/n-type ZnO heterostructure and its enhanced photocatalytic activity. Scr Mater 69(5):417–419
27. Liu Y, Li G, Mi R, Deng C, Gao P (2014) An environment-benign method for the synthesis of p-NiO/n-ZnO heterostructure with excellent performance for gas sensing and photocatalysis. Sens Actuators B Chem 191:537–544
28. Kizler B, Peker SM (2016) Synthesis of TiO_2 coated ZnO nanorod arrays and their stability in photocatalytic flow reactors. Thin Solid Films 605:232–242. https://doi.org/10.1016/j.tsf.2015.11.083
29. Poongodi G, Kumar RM, Jayavel R (2015) Structural, optical and visible light photo-catalytic properties of nanocrystalline Nd doped ZnO thin films prepared by spin coating method. Ceram Int 41:4169–4175
30. Sarma B, Deb SK, Sarma BK (2016) Photoluminescence and photocatalytic activities of Ag/ZnO metal-semiconductor heterostructure. In: Journal of physics: conference series, pp 1–7
31. Pauporte´ T, Rathouský J (2007) Electrodeposited mesoporous ZnO thin films as efficient photocatalysts for the degradation of dye pollutants. J Phys Chem C 111:7639–7644
32. Kaneva N, Ponomareva A, Krasteva L, Dimitrov D, Bojinova A, Papazova K, Suchaneck G, Moshnikov V (2013) Surface and photocatalytic properties of nanostructured ZnO thin films doped with iron. Bul Chem Commun 45(4):635–643
33. Brillson LJ, Lu Y (2011) ZnO Schottky barriers and Ohmic contacts. J Appl Phys 109:121301–121333
34. Kosmulski M (2009) Compilation of PZC and IEP of sparingly soluble metal oxides and hydroxides from literature. Adv Colloid Interface Sci 152:14–25
35. Balachandran S, Swaminathan M (2012) Facile fabrication of heterostructured Bi_2O_3–ZnO photocatalyst and its enhanced photocatalytic activity. J Phys Chem C 116:26306–26312
36. Chen H, Wageh S, Al-Ghamdi AA, Wang H, Yu J, Jiang C (2019) Hierarchical C/NiO-ZnO nanocomposite fibers with enhanced adsorption capacity for Congo red. J Coll and Int Sci 537:736–745
37. Kakazey M, Vlasova M, Juarez-Arellano EA, Torchynska T, Basiuk VA (2016) Defect states and morphological evolution in mechanically processed ZnO+: X C nanosystems as studied by EPR and photoluminescence spectroscopy. RSC Adv 6:58709–58722
38. Richters JP, Voss T, Kim DS, Scholz R, Zacharias M (2008) Enhanced surface-excitonic emission in ZnO/Al_2O_3 core–shell nanowires. Nanotechnology 19(305202):1–4
39. Echresh A, Chey CO, Shoushtari MZ, Nur O, Willander M (2014) Tuning the emission of ZnO nanorods based light emitting diodes using Ag doping. J Appl Phys 116:193104-1–193104-8
40. Vempati S, Mitra J, Dawson P (2012) One-step synthesis of ZnO nanosheets: a blue-white fluorophore. Nanoscale Res Lett 7(August):1–10
41. Yang A, Yang Y, Zhang Z, Bao X, Yang R, Li S, Sun L (2013) Photoluminescence and defect evolution of nano-ZnO thin films at low temperature annealing. Sci China Technol Sci 56(1):25–31
42. Shabnam, Kant CR, Arun P (2010) Controlling the photoluminescence of ZnO: Si nano-composite films by heat-treatment. Mater Res Bull 45:1368–1374
43. Ha B, Ham H, Lee CJ (2008) Photoluminescence of ZnO nanowires dependent on O_2 and Ar annealing. J Phys Chem Solids 69:2453–2456
44. Rodrigues J, Holz T, Allah RF, Gonzalez D, Ben T, Correia MR, Monteiro T, Costa FM (2015) Effect of N_2 and H_2 plasma treatments on band edge emission of ZnO microrods. Sci Rep 5:1–9. https://doi.org/10.1038/srep10783
45. Urgessa ZN, Botha JR, Eriksson MO, Mbulanga CM, Dobson SR, Tankio Djiokap SR, Karlsson KF, Khranovskyy V, Yakimova R, Holtz PO (2014) Low temperature near band edge recombination dynamics in ZnO nanorods. J Appl Phys 116(12):123506-1 - 123506-10

46. Zhu Q, Xie C, Li H, Yang C, Zhang S, Zeng D (2014) Selectively enhanced UV and NIR photoluminescence from a degenerate ZnO nanorod array film. J Mater Chem C 2(23):4566–4580
47. Manjula N, Balu AR, Usharani K, Raja N, Nagarethinam VS (2016) Enhancement in some physical properties of spray deposited CdO:Mn thin films through Zn doping towards optoelectronic applications. Optik 127(16):6400–6406. https://doi.org/10.1016/j.ijleo.2016.04.129
48. Lee HB, Ginting RT, Tan ST, Tan CH, Alshanableh A, Oleiwi HF, Yap CC, Jumali MHH, Yahaya M (2016) Controlled defects of fluorine-incorporated ZnO nanorods for photovoltaic enhancement. Sci Rep 6:1–11
49. Drouilly C, Krafft JM, Averseng F, Casale S, Chizallet C, Lecocq V, Vezin H, Lauron-Pernot H, Costentin G (2012) ZnO oxygen vacancies formation and filling followed by in situ PL and in situ EPR. J Phys Chem C 116:21297–21307
50. Gheisi AR, Neygandhi C, Sternig AK, Carrasco E, Marbach H, Thomele D, Diwald O (2014) O_2 adsorption dependent photoluminescence emission from metal oxide nanoparticles. Phys Chem Chem Phys 16:23922–23929
51. Li M, Xing G, Ah Qune LFN, Xing G, Wu T, Huan CHA, Zhang X, Sum TC (2012) Tailoring the charge carrier dynamics in ZnO nanowires: the role of surface hole/electron traps. Phys Chem Chem Phys 14:3075–3082
52. Lee Y-M, Yang H-W, Huang C-M (2012) Effect of rapid thermal annealing on the structural and electrical properties of solid ZnO/NiO heterojunctions prepared by a chemical solution process. J Phys D Appl Phys 45:225302-1–225302-7
53. Reshchikov MA, Wessels BW (1999) Behavior of 2.8- and 3.2-eV photoluminescence bands in Mg-doped GaN at different temperatures and excitation densities. Phys Rev B 59(20):176–183
54. Li JM, Wu JJ, Han XX (1998) Theory of interface roughness scattering in quantum wells. Semicond Sci Technol 13:709–713
55. Kaneva N, Stambolova I, Blaskov V, Dimitriev Y, Vassilev S, Dushkin C (2010) Photocatalytic activity of nanostructured ZnO films prepared by two different methods for the photoinitiated decolorization of malachite green. J Alloy Compd 500:252–258
56. Cheng Q, Benipal MK, Liu Q, Wang X, Crozier PA, Chan CK, Nemanich RJ (2017) Al_2O_3 and SiO_2 atomic layer deposition layers on ZnO photoanodes and degradation mechanisms. Appl Mater Interfaces 9:16138–16147
57. Hosseiny S, Wessling M (2011) Ion exchange membranes for vanadium redox flow batteries. In: Advanced membrane science and technology for sustainable energy and environmental applications
58. Sokol AA, French SA, Bromley ST, Catlow CRA, Van Dam HJ, Sherwood P (2007) Point defects in ZnO. Faraday Discuss 134:267–282
59. Jaegermann W, Klein A, Mayer T, Thissen A (2008) Photoelectron spectroscopy in materials science and physical chemistry: analysis of composition, chemical bonding and electronic structure of surfaces and interfaces. Bunsen-Magazin 10(4):124–139
60. Siol S, Hellmann JC, Tilley SD, Graetzel M, Morasch J, Deuermeier J, Jaegermann W, Klein A (2016) Band alignment engineering at Cu_2O/ZnO heterointerfaces. Appl Mater Interfaces 8:21824–21831
61. Klein A (2013) Transparent conducting oxides: electronic structure–property relationship from photoelectron spectroscopy with in situ sample preparation. J Am Ceram Soc 96(2):331–345
62. Kraut EA, Grant RW, Waldrop JR, Eowalczyk SP (1980) Precise determination of the valence-band edge in X-ray photoemission spectra: application to measurement of semiconductor interface potentials. Phys Rev Lett 44(24):1620–1623
63. Shi L, Wang F, Wang Y, Wang D, Zhao B, Zhang L, Zhao D, Shen D (2016) Photoluminescence and photocatalytic properties of rhombohedral $CuGaO_2$ nanoplates. Sci Rep 6:1–10. https://doi.org/10.1038/srep21135
64. Qi K, Cheng B, Yu J, Ho W (2017) Review on the improvement of the photocatalytic and antibacterial activities of ZnO. J Alloy Compd 727:792–820. https://doi.org/10.1016/j.jallcom.2017.08.142

Affiliations

Shanmugapriya Periyannan[1,2] · Laura Manceriu[1] · Ngoc Duy Nguyen[3] · Andreas Klein[2] · Wolfram Jaegermann[2] · Pierre Colson[1] · Catherine Henrist[1] · Rudi Cloots[1]

✉ Shanmugapriya Periyannan
speriyannan@uliege.be; periyannan@surface.tu-darmstadt.de; priya1988infotech@gmail.com

[1] GREENMAT-LCIS, CESAM Research Unit, Institute of Chemistry, Universite de Liege, B6, Sart Tilman, 4000 Liege, Belgium

[2] Surface Science Division, Institute of Materials Science, Technische Universitat Darmstadt, Otto-Berndt-Strasse 3, 64287 Darmstadt, Germany

[3] SPIN, CESAM Research Unit, Institute of Physics, Universite de Liege, B5, Sart Tilman, 4000 Liege, Belgium